Evolution of mineral accessible surface area induced

by geochemical reactions

- 3 Fanqi Qin, Md. Fahim Salek, Parisa Asadi, Lauren E. Beckingham*
- 4 Department of Civil and Environmental Engineering, Auburn University,
- 5 Auburn, AL, 36849
- 6 *Corresponding Author: leb0071@auburn.edu

7 Abstract

16

1

- Mineral dissolution and precipitation reactions occur in a wide range of porous media systems,
 driven by deviations from an equilibrium between solid and fluid phases. Reactions occur at
- 10 mineral surfaces in contact with reactive fluids or accessible mineral surface areas. These
- mineral surface areas can be determined using a multi-scale imaging approach and have been
- 12 shown to improve the simulation of mineral reaction rates in porous media compared to other
- 13 estimates of reactive surface area. As reactions progress, mineral surface area evolves, and
- 14 reactive transport simulations often use a simplified model assuming spherical grains to
- 15 estimate mineral surface area evolution. This, however, does not depict the evolution of
 - reactive surfaces in porous media systems with varying mineral accessibility. This work aims

to quantitatively assess the evolution of accessible mineral surface area in porous media for a multi-mineralic system undergoing mineral dissolution reactions induced by acid exposure. Before and after the reaction, accessible mineral surface areas are determined from 2D Scanning Electron Microscopy, and 3D X-ray Computed Tomography imaging of a sandstone sample. The quantified evolution of accessible surface area is compared to the calculated mineral surface area evolution using current approaches. Results show an overall increase in total surface area due to reaction; however, individual mineral surface areas may increase or decrease. Variation is observed in mineral surface area values measured from imaging and equations used in models. The evolution of mineral surface area is largely impacted by the total surface area as well as the pore connectivity rather than porosity and volume fraction evolution.

- Keywords: Mineral Accessible Surface Area, Core Flood Experiment, Mineral Surface Area
 Evolution, Scanning Electron Microscopy, Geochemical Reactions
 - 1. Introduction

Mineral dissolution and precipitation reactions, such as those resulting from natural weathering or CO₂ sequestration, can be impacted by temperature, pH, salinity, mineral reactive surface area, etc. ^{1–9}. As mineral reactions progress, formation properties, including porosity and permeability, can be altered as the pore structure and pore connectivity evolve ^{10–15}. This, in turn, could impact the ongoing reactions. Among all these constantly changing

factors, the mineral reactive surface area may also evolve as the reaction proceeds ^{16–20}. When pore connectivity increases ¹⁷ or mineral grains disaggregate ^{21,22}, the mineral reactive surface area could increase. Alternatively, fine mineral grains with a large surface area experiencing rapid dissolution ^{21,23} could decrease the overall mineral reactive surface area.

The evolution of mineral reactive surface area during mineral reactions is not well understood. In reactive transport simulations, the evolution of mineral surface area is typically treated assuming a particle geometry and updating mineral surface area at each time step based on the change in mineral volume fraction and porosity. For example, in CrunchFlow ²⁴, a modeling tool developed for multicomponent reactive flow and transport, the reactive surface area of the primary minerals is given by,

$$A_{m} = A_{m,0} \begin{cases} \left[\left(\frac{\phi}{\phi_{0}} \right) \left(\frac{\phi_{m}}{\phi_{m,0}} \right) \right]^{2/3} & dissolution \\ \left[\frac{\phi}{\phi_{0}} \right]^{2/3} & precipitation \end{cases}$$
 (1)

where A_m is the mineral reactive surface area, $\phi_{m,\theta}$ is the initial volume fraction of the mineral m, and ϕ_{θ} refers to the initial mineral porosity. The reactive surface areas of secondary minerals, those that precipitate as the simulation progresses, are calculated using a similar approach as given by,

51
$$A_{m} = A_{m,0} \begin{cases} \left[\left(\frac{\phi}{\phi_{0}} \right) \phi_{m} \right]^{2/3} & dissolution \\ \left[\frac{\phi}{\phi_{0}} \right]^{2/3} & precipitation \end{cases}$$
 (2)

Similar relationships have been used in other studies ^{16,25,26}, where changing mineral surface area is associated with changing mineral abundance and porosity. These relationships are based on the assumption that mineral grains are spherical and smooth, and mineral surface area

decreases with decreasing grain volume. This may reflect the mineral surface area change in some cases (e.g., some disaggregated samples); however, it does not necessarily reflect the surface area of consolidated samples or account for mineral surface roughness. Additionally, calculating mineral surface area assuming grains are spherical implies the entire surface is involved in the reaction, while in reality, it is highly likely that only a fraction of the surface is actively involved in the reactions due to limitations in accessibility 27-30 or variations in surface site reactivity 31,32. Experimental studies have examined the evolution of mineral surface area during reactions. For instance, Mouzakis et al.³³ studied the evolution of shale caprock porosity with respect to CO₂-brine-mineral reactions and found that the total surface area and connected surface area increase when there is an obvious increase in mineral porosity and connected porosity. Noiriel et al.21 observed that the reactive surface area of limestone (micrite and sparite) increased during an acidic water flow-through experiment, and the change of reactive surface area was impacted by the mineral spatial distribution and pore connectivity. However, it is challenging to determine mineral reactive surface areas since only a fraction of the surface might be actively involved (reactive) during the reactions ^{29,34}. Recent work noted that accessible mineral surface area, which reflects the proportion of mineral surfaces in contact with reactive fluids, may better reflect the mineral reactive surface area in consolidated porous media 9,29. These accessible mineral surface areas can be quantified using a multi-scaling imaging approach ^{28,35–39}. This surface area was able to better reflect mineral dissolution rates in a consolidated volcanogenic sandstone sample as compared with

55

56

57

58

59

60

61

62

63

64

65

66

67

68

69

70

71

72

73

74

other commonly used approaches that estimate reactive surface area based on spherical grains with largely arbitrary corrections for surface roughness and reactivity ²⁹.

While accessible mineral surface areas have shown promise for improving simulations of mineral reaction rates in porous media, it is still unknown how accessible mineral surface areas evolve as reactions progress. This work aims to capture and quantify the evolution of accessible mineral surfaces to improve understanding of surface area evolution and simulate mineral reactions and reaction rates in porous media. Here, accessible surface areas are measured using an imaging analysis approach before and after the reaction with acidic fluids in flow-through dissolution experiments. The relationship between mineral accessible surface area, mineral volume fraction, and porosity is considered for different mineral species and compared to mineral surface areas calculated using the approach typically used in reactive transport simulations (equation 1).

2. Materials and methods

2.1 Sample characterization and preparation

Two sandstone core samples from the Kentucky and Bandera Grey formations were selected for core-flood experiments and image analysis. Samples were provided by Kocurek Industries. Both core samples were 0.5 inch in diameter and 1 inch in length. The expected porosity was 20% for the Bandera Grey sample and 14% for the Kentucky sample (data provided by Kocurek Industries). Both samples were predominantly composed of quartz, with other mineral species,

including feldspar, carbonate, and clay minerals accounting for 12 to 15% of the composition, respectively (Kocurek Industries). Detailed mineralogy is given in Table 1.

Unreacted and reacted core samples were cut into thick sections of 0.5-inch diameter and 0.5 cm thickness for 2D scanning electron microscopy (SEM) imaging. One side of each sample was polished and impregnated with clear epoxy. The preparation was performed by Applied Petrographic Services. Inc (Westmoreland, Pennsylvania). Sample preparation for 2D imaging is by nature, a destructive process. As such, the preparation of polished sections of the sample before and after the experiments to image the same location is not feasible. Instead, unreacted thick sections were created from core samples not used in the core-flood experiments.

Table 1. Mineral composition (wt%) of sandstone sample from XRD data provided by Kocurek Industries.

Mineral	Quartz	Albite	Microcline	Dolomite	Kaolinite	Illite	Chlorite
Kentucky sandstone	66	17	3	-	-	14	-
Bandera Gray sandstone	59	12	0	15	3	10	1

2.2 Mineral properties quantification

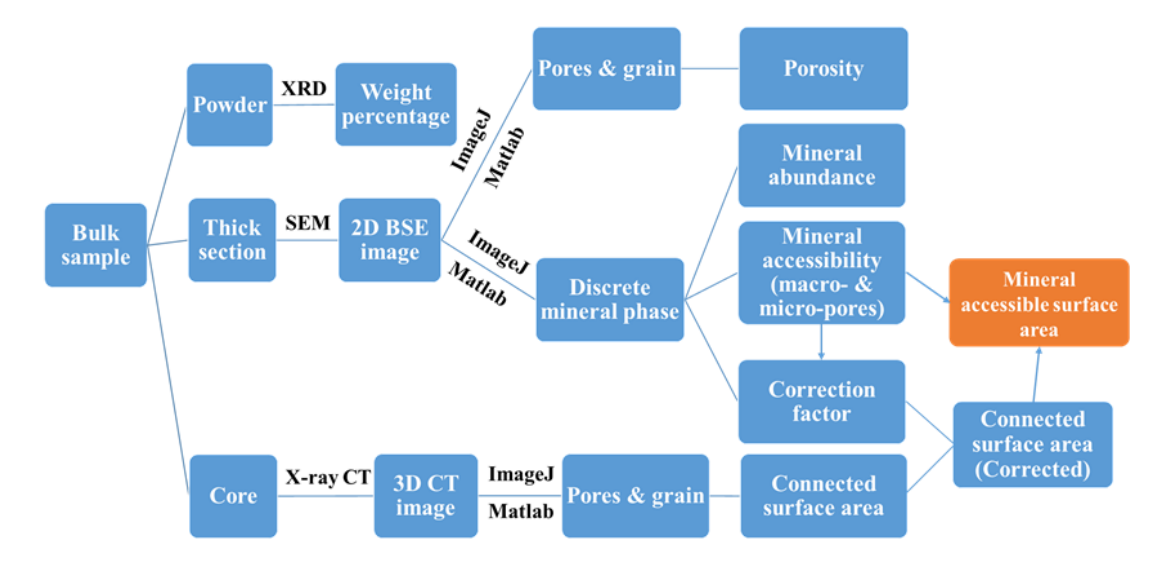


Figure 1. Workflow of mineral properties (porosity, abundance, accessibility, accessible surface area) quantification.

Mineral properties, including porosity, mineral abundance, accessibility, and accessible surface areas, were quantified from unreacted and reacted samples using a multi-scale imaging and analysis approach (Figure 1). Thick sections were imaged using 2D SEM using a ZEISS EVO 50VP scanning electron microscope at the Auburn University Research Instrumentation Facility (AURIF) at Auburn University. Backscattered electron (BSE) and energy dispersive x-ray spectroscopy (EDS) images were captured with a beam intensity of 20 kV and a working distance of 8.5 mm. Pores and grains in SEM BSE images were first segmented by applying the thresholding approach proposed by Peters ²⁷. The porosity was then calculated by pixel counting by,

120
$$porosity = \frac{number\ of\ pore\ pixels}{total\ number\ of\ pixels} \tag{3}.$$

Following the initial segmentation, each mineral phase was identified by combining BSE images with EDS elemental maps. The discrete mineral phases were then registered and assigned different colors to create a mineral-phase segmented image. Mineral abundance and accessibility were then calculated from the maps. Mineral abundance reflects the fraction of each discrete mineral phase in relation to the total mineral volume fraction (pores not included). Abundances were calculated by pixel counting by

127 mineral abundance of phase
$$i = \frac{pixels\ of\ phase\ i}{total\ mineral\ pixels} * 100\%$$
 (4)

Mineral accessibility is defined as the mineral surface which is in direct contact with the pore space and was calculated by counting the number of mineral pixels for each specific mineral phase which are adjacent to pore pixels as given by,

131 mineral accessibility of phase
$$i = \frac{interfacial\ pixels\ of\ phase\ i}{total\ interfacial\ pixels}*100\%$$
 (5).

The accessible mineral surface area for each phase was calculated for each mineral phase following the 2D and 3D imaging approach proposed by Landrot et al.²⁸. 3D X-ray CT images were captured using a ZEISS Xradia 620 Versa X-ray computed tomography microscope at Auburn University. The beam intensity was set to be 100 keV with 8 seconds exposure time, and a total of 3601 projections were taken for each sample at a voxel resolution of 2 microns. The reconstruction of the images was performed by the automated reconstruction software provided by ZEISS. The connected pore regions within this 3D image were identified using a marching cube and burning algorithms, from which the total connected surface area was calculated based on a mesh defined on the associated mineral surfaces. The accessible mineral

surface area of each phase, *ASAi*, was then calculated by multiplying the accessibility of each mineral phase, determined from the 2D SEM imaging analysis, by the total connected surface area as given by,

144
$$ASA_i = accessibility_i * total connected surface area$$
 (6)

Lastly, a correction factor (CF) was calculated to account for the estimation error of connected surface area resulting from resolution differences in the 2D SEM BSE image and 3D X-ray CT images. The resolution of the SEM BSE image was reduced to match the resolution of X-ray CT images. Then the number of connected interfacial pixels, those adject to connected porosity, in the two images was determined. The correction factor was calculated as the number of connected interfacial pixels in the original image divided by the number of connected interfacial pixels in the resolution-reduced image as given by,

$$CF = \frac{connected\ interfacial\ pixels\ in\ original\ SEM\ BSE\ image}{connected\ interfacial\ pixels\ in\ reduced\ resolution\ image}} \tag{7}$$

This was then multiplied by the connected surface area to get the corrected connected surface area. As 3D X-ray CT imaging is nondestructive, 3D X-ray CT images of the core samples were captured for the same area of interest before and after the reaction.

2.3 Core-flood dissolution experiments

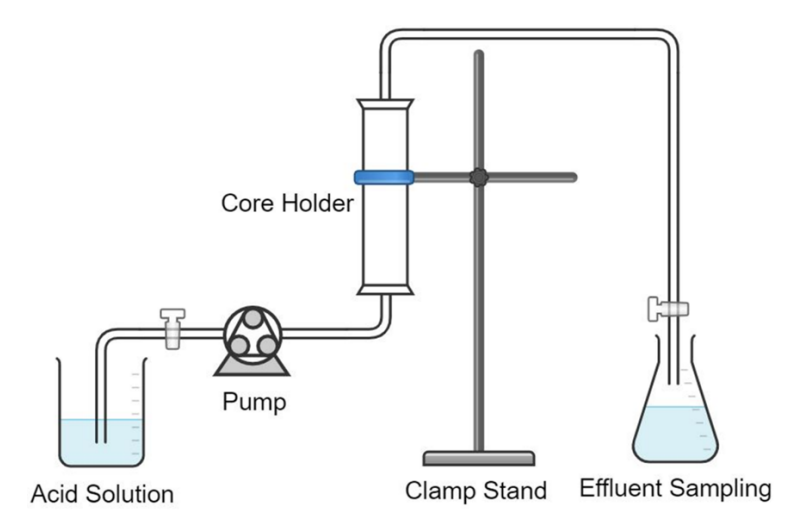


Figure 2. Experimental setup diagram of a single-phase core-flood through dissolution experiment.

The core-flood dissolution experiments were carried out on core samples from each formation. The experimental setup is shown in Figure 2. Experiments were conducted at room temperature (25 °C) with 0.01 M hydrochloric acid (pH = 2) used as the reacting fluid. A CHEM_TECH peristaltic chemical metering pump was used to provide a constant flow rate of 1 ml/min. A 3D-printed core holder was used for the experiment. It was designed in Autodesk Fusion 360 and printed using an Anycubic Photon SLA 3D resin printer. The core samples were wrapped in a heat-shrinkable tube which was then placed in the 3D-printed core holder. The heat shrink tubing was epoxied to the inner wall of the core holder to prevent flow. The core was first flushed with deionized water at a flow rate of 1 ml/min for 24 hours to saturate the sample, followed by 0.01 M hydrochloric acid. This corresponds to a total of 9,293 and 13,190 pore volumes (PVs) of HCl solution flowed through Kentucky and Bandera Grey core sample, respectively, over one week (168 hours) and two weeks (336 hours) experimental

periods.. At the end of the experiments, deionized water was used again to flush out the acid residue. Effluent samples were periodically collected and evaluated with an inductively coupled plasma–optical emission spectrometer (ICP-OES) for the concentration of the following ions: potassium (K+), sodium (Na+), magnesium (Mg2+), calcium (Ca2+), iron (Fe2+/Fe3+) and aluminum (Al3+). The ICP-OES analysis was carried out on a Varian 710ES ICP-OES at Auburn University.

3. Results

3.1 Image segmentation and mineral property quantification

3.1.1 Unreacted samples

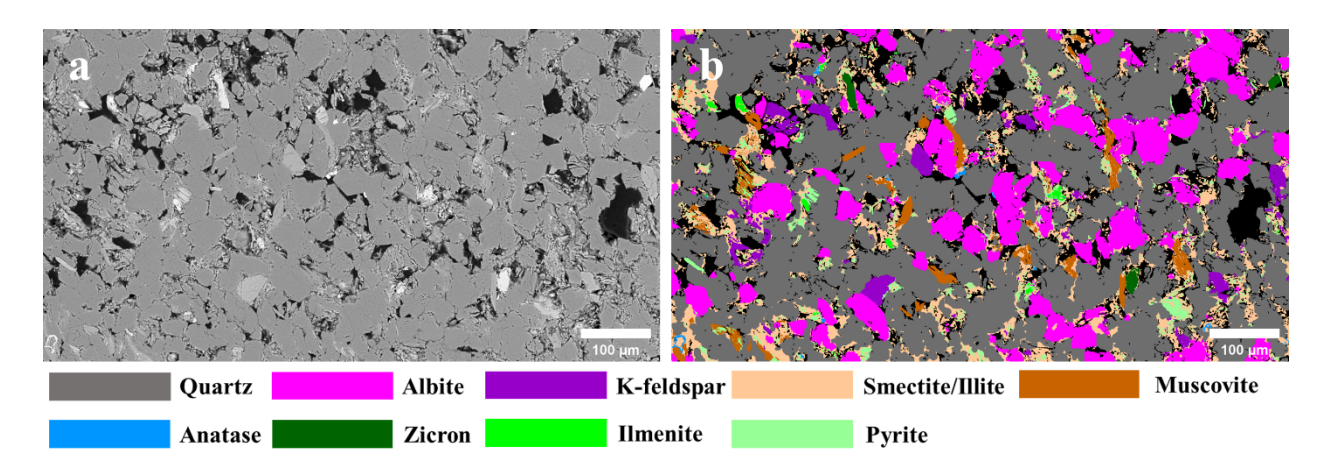


Figure 3. a) 2D SEM BSE image of the unreacted Kentucky sample thick section captured under a resolution of 0.44 μ m; b) discrete mineral phase map with nine mineral phases identified and segmented, each color corresponding to a different mineral. Reproduced with permission from ref (40) ⁴⁰. Copyright 2022 ACS Publications.

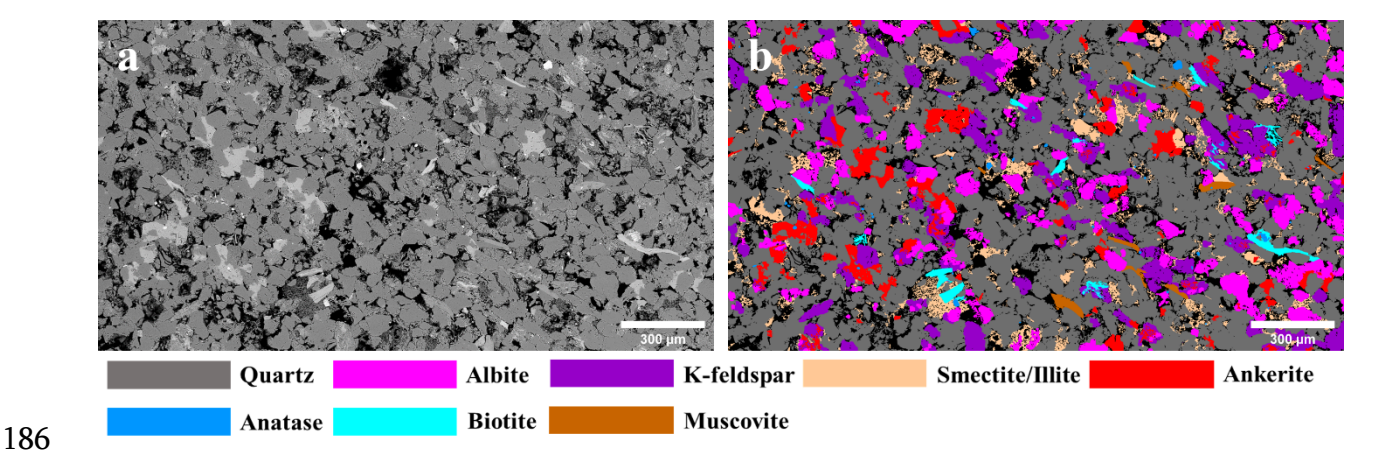


Figure 4. a) 2D SEM BSE image of the unreacted Bandera Grey sample thick section captured under a resolution of 0.74 μ m; b) mineral phase segmented map with eight minerals identified in the area of interest, each mineral expressed in a unique color. Reproduced with permission from ref (40) ⁴⁰. Copyright 2022 ACS Publications.

Table 2. Mineral properties of the unreacted samples were determined from 2D SEM BSE images and 3D X-ray CT images. The accessible surface area of smectite/illite, muscovite, and biotite cannot be directly measured through the images captured. The abundances are measured in volume percentage.

Sample	Mineral	Abundance (v%)	Accessibility (v%)	Accessible surface area (m²/g)
	Quartz	62.58	33.66	4.73 x10 ⁻⁰²
Kentucky	Albite	16.79	10.05	1.41 x10 ⁻⁰²
	K-feldspar	2.92	3.54	4.98 x10 ⁻⁰³
	Smectite/Illite	11.73	47.54	NA
	Muscovite	2.55	2.76	NA
	Ilmenite	0.29	0.37	5.02 x10 ⁻⁰⁴

	Pyrite	2.60	1.76	2.48 x10 ⁻⁰³
	Anatase	0.17	0.14	1.97 x10 ⁻⁰⁴
	Zircon	0.37	0.18	2.53 x10 ⁻⁰⁴
	Quartz	63.46	60.91	3.85 x10 ⁻⁰²
	K-feldspar	12.12	5.59	3.53 x10 ⁻⁰³
	Albite	10.22	6.59	4.16 x10 ⁻⁰³
Bandera Grey	Ankerite	5.69	0.71	4.48 x10 ⁻⁰⁴
	Smectite/Illite	6.39	26.09	NA
	Muscovite	0.69	0.00	NA
	Biotite	1.14	0.00	NA
	Anatase	0.29	0.10	6.31 x10 ⁻⁰⁵

2D BSE images of the unreacted samples and their corresponding mineral-segmented maps are shown in Figures 3 and 4, and calculated properties are given in Table 2. Nine mineral species were identified in the BSE image of the Kentucky sample (Figure 3), where quartz has the highest abundance (62.58%), followed by albite, with an abundance of 16.79%. The clay content of the Kentucky sample is also high, where 11.73% of the sample is composed of smectite and illite mixture. The abundances of other mineral phases are all below 3%. Even though quartz is the most dominant phase, the accessibility of quartz is only 33.36%, whereas the accessibility of smectite/illite is 47.54%. This is because clay minerals commonly exist as coating or bridging phases on/between the surfaces of other mineral grains, which limits the accessibility of other mineral species. The abundances of other minerals are less than 3%.

As for Bandera Grey, eight mineral phases were identified and segmented in the area of interest (Figure 4). Quartz is the predominated phase with 63.46% abundance, the abundances of K-feldspar and albite are calculated to be 12.12% and 10.22%. One carbonate mineral, ankerite, is also found to be present with an abundance of 5.69%. The clay minerals found in the area of interest are mainly composed of smectite and illite mixture. The abundances of other minerals are all below 2%. Quartz has the highest accessibility (60.91%), followed by smectite/illite (26.09%). Although the abundances of ankerite and smectite/illite are close, the accessibility of ankerite (0.71%) is significantly lower than smectite/illite. The accessibility of the two feldspar minerals – K-feldspar and albite are calculated to be 5.59% and 6.59%, respectively.

Table 3. Porosity and connected surface area determined from 3D X-ray CT images and calculated pore volume of the samples before and after the experiment.

Sample	Porosity determined from CT image (%)	Connected Porosity from CT image (%)	Total Pore Volume (cm³)	Connected surface area (m²/g)	Corrected Connected surface area (m²/g)
Kentucky (unreacted)	10.73	7.95	1.08	0.015	0.141
Kentucky (reacted)	13.23	10.73	1.34	0.020	0.228
Bandera Grey (unreacted)	15.12	14.17	1.53	0.018	0.063
Bandera Grey (reacted)	20.87	20.04	2.11	0.023	0.085

220

221

222

223

224

225

226

227

228

229

230

231

232

233

234

235

236

237

238

The original and segmented 3D X-ray CT images can be found in the supplementary materials (Figures S1 and S2). The porosity of the unreacted Kentucky sample, determined from the X-ray CT image is 10.73% (Table 3), and 74% of the pores are connected (connected porosity 7.95%). In comparison, the porosity computed from the segmented 2D SEM image is 13.25%. This discrepancy is likely due to the lower resolution of the X-ray CT images. The calculated accessible surface areas for each mineral, determined by multiplying mineral accessibility by the 3D connected surface area corrected for resolution discrepancies, are given in Table 2 and vary up to 2 orders of magnitude (Table 2). The accessible surface area of quartz and albite are 4.73 x10⁻⁰² and 1.41 x10⁻⁰² m²/g, respectively. For other mineral species, the calculated accessible surface areas fall within the range of 1.97 x10⁻⁰⁴ to 4.98 x10⁻⁰³ m²/g. It should be noted that the resolution of the images captured here is inadequate to measure the surface area of clay minerals and minerals like muscovite/biotite that have many small-scale features on the surface. As such, the accessible surface areas of these mineral phases are not discussed here. The porosity calculated from the segmented 3D CT image of the unreacted Bandera Grey sample is 15.12% which is similar to the porosity determined from the 2D SEM images of 15.31%. The connected porosity is 14.17%, which is 94% of the total porosity. The pore volume of the unreacted Bandera Grey core sample calculated from the porosity is 1.53 cm³, which is approximately 1.5 times the pore space of the Kentucky sample (1.08 cm³). The accessible surface areas of each mineral phase, computed via analysis of the 3D connected surface area

from extracted cuboids in the 3D image and adjusted by the correction factor, are given in Table 2 and vary up to two orders of magnitude. Quartz has the highest accessible surface area $(3.85 \text{ x} 10^{-02} \text{ m}^2/\text{g})$, followed by two feldspar minerals – K-felspar $(3.53 \text{ x} 10^{-03} \text{ m}^2/\text{g})$ and albite $(4.16 \text{ x} 10^{-03} \text{ m}^2/\text{g})$. The accessible surface area of ankerite is calculated to be $4.48 \text{ x} 10^{-04} \text{ m}^2/\text{g}$ and $6.31 \text{ x} 10^{-05} \text{ m}^2/\text{g}$ for anatase.

3.1.2 Reacted samples

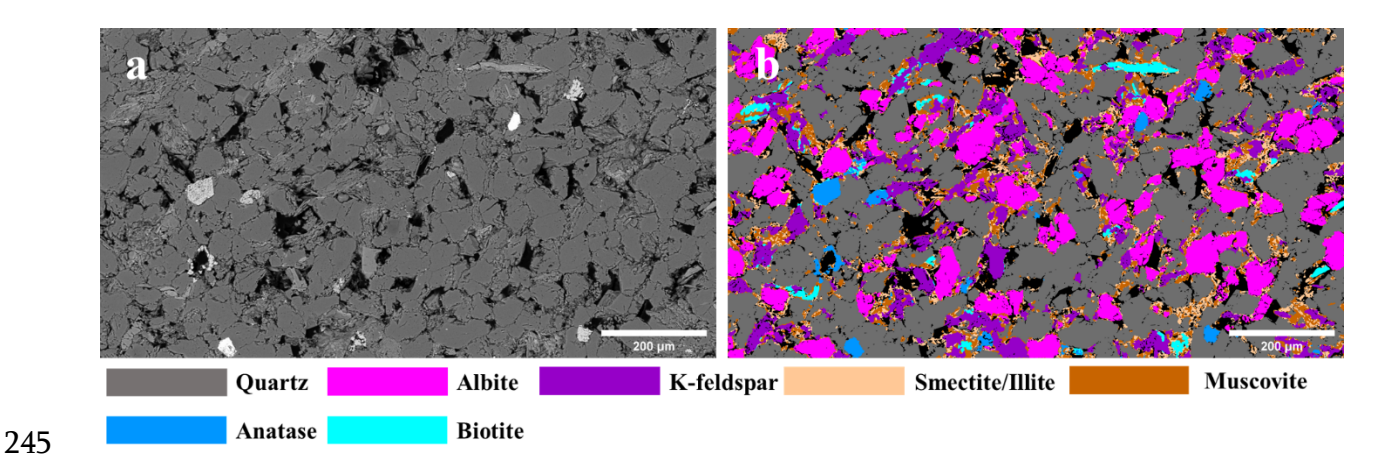


Figure 5. A) 2D SEM BSE image of the reacted Kentucky sample thick section captured under a resolution of 0.30 μ m; b) discrete mineral phase map with six mineral phases identified and segmented, each color corresponding to one mineral phase.

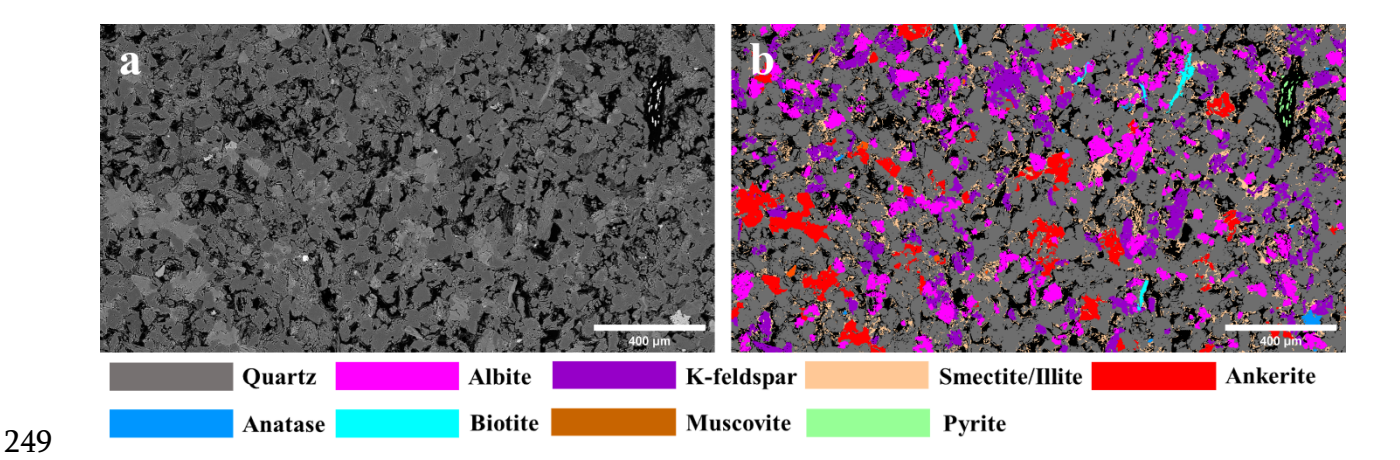


Figure 6. A) 2D SEM BSE image of the reacted Bandera Grey sample thick section captured under a resolution of 0.74 μ m; b) mineral phase segmented map with nine minerals identified in the area of interest, each mineral phase expressed in a unique color.

2D BSE images of the reacted samples and the segmented images are shown in Figures 5 and 6. Seven mineral species were identified in the reacted Kentucky sample, and each mineral is marked in a unique color. As the 2D imaging technique is by nature a destructive method, the 2D images captured here are not from the same place or sample as the unreacted images; thus, some discrepancies are expected. However, it should be noted that the considered area is larger than the representative elementary volume (REV) for the sample as determined by analyzing the sample porosity in images of increasing size. In general, quartz and albite are still the two most abundant phases in the reacted Kentucky sample. Pyrite was observed in the unreacted sample but not observed in the reacted sample. Biotite was evident in the reacted sample but was absent in the unreacted sample.

Overall, similar observations in abundance versus accessibility were observed in the reacted sample. While quartz still has the highest abundance after reaction, the smectite/illite clay

mixture has the highest accessibility. The accessibility of quartz is reduced as compared to its abundance, while smectite/illite accessibility is enhanced as compared to its abundance, which is the same as observed for mineral accessibility before reaction. However, the accessible surface area for the quantifiable minerals all increased after the reaction. The accessible surface area of quartz and albite are three times higher than before the reaction, and the accessible surface areas of K-feldspar and anatase have more than one order of magnitude increase.

In the segmented reacted Bandera Grey sample image, a total of 10 mineral species were identified. The abundance distributions calculated from the sample before and after the reaction are very close. There is no distinct change in the ankerite abundance, where the

identified. The abundance distributions calculated from the sample before and after the reaction are very close. There is no distinct change in the ankerite abundance, where the abundance in the unreacted sample was 5.69% and 5.56% in the reacted sample. Quartz remains the most accessible phase with an accessibility of 58%, followed by smectite/illite with 33.22% accessibility. As with the unreacted sample, the accessibility of smectite/illite is enhanced compared with its abundance. The accessible surface area of all mineral phases identified in the Bandera Grey sample after reaction slightly decreased except for quartz, which has increased in accessible surface area. All such changes in the accessible surface area in Bandera Grey are less than one order of magnitude.

Table 4. Mineral properties of the reacted samples determined from 2D SEM BSE images and 3D X-ray CT images. The accessible surface area of smectite/illite, muscovite, and biotite cannot be directly measured through the images captured. The abundances are measured in volume percentage.

Sample	Mineral	Abundance (v%)	Accessibility (v%)	Accessible surface area (m²/g)
	Quartz	54.24	27.42	6.28 x10 ⁻⁰²
	Albite	16.00	8.85	2.03 x10 ⁻⁰²
	K-feldspar	11.82	11.18	2.56 x10 ⁻⁰²
	Smectite/Illite	6.92	41.05	NA
Kentucky	Muscovite	8.06	10.20	NA
Remarky	Anatase	1.52	0.57	1.31 x10 ⁻⁰³
	Biotite	1.44	0.74	NA
	Pyrite	0	0	0
	Ilmenite	0	0	0
	Zircon	0	0	0
	Quartz	66.60	58.08	4.95 x10 ⁻⁰²
	K-feldspar	10.30	2.89	2.46 x10 ⁻⁰³
	Albite	9.45	4.03	3.43 x10 ⁻⁰³
	Ankerite	5.56	0.08	6.81 x10 ⁻⁰⁵
Bandera	Smectite/Illite	7.27	33.22	NA
Grey	Muscovite	0.02	0	NA
	Biotite	0.35	0.0046	NA
	Anatase	0.23	0.01	8.51 x10 ⁻⁰⁶
	Pyrite	0.09	1.68	1.41 x10 ⁻⁰³
	Apatite	0.11	0	0

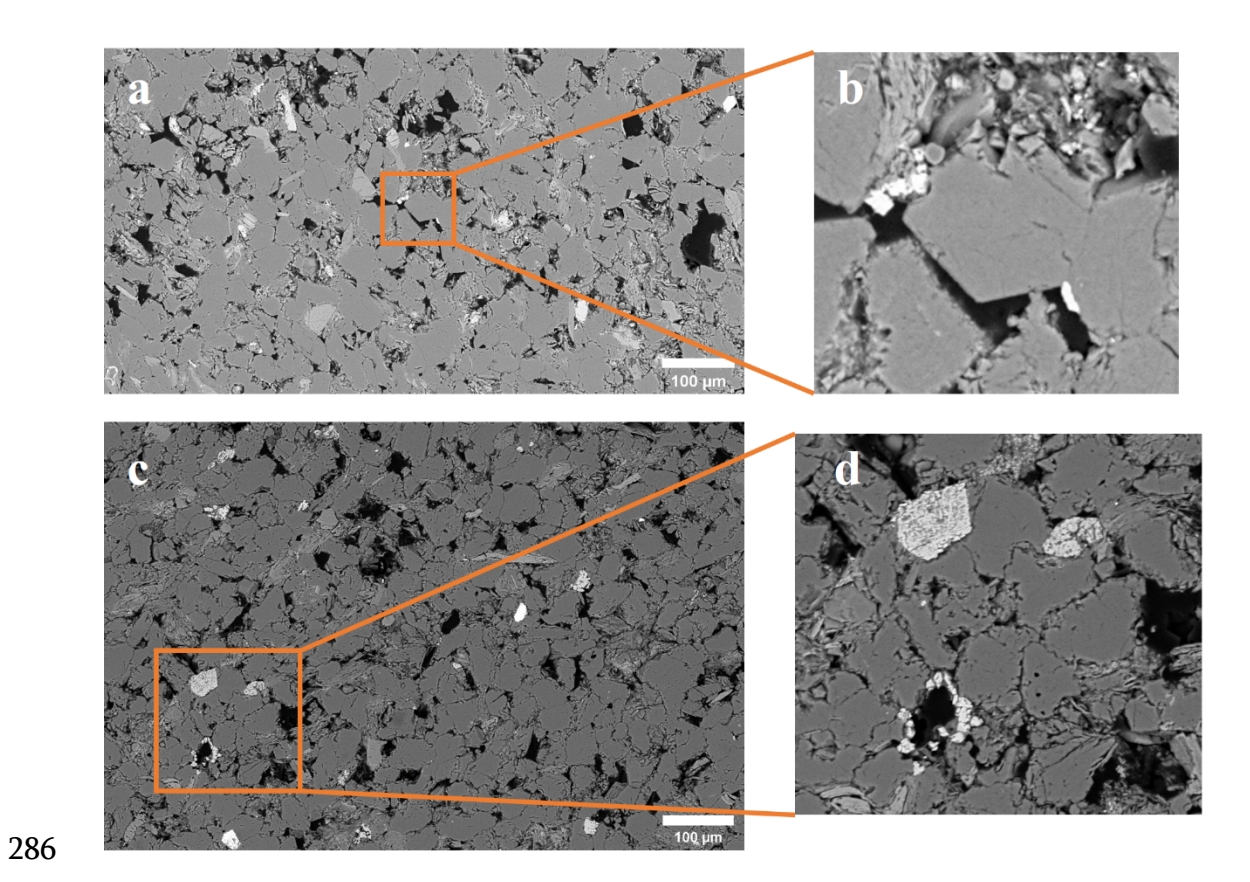


Figure 7. 2D BSE images of unreacted and reacted Kentucky sample thick sections: a) BSE image of the unreacted sample, captured under a resolution of 0.44 μ m; b) enlarged image of unreacted grain surfaces; c) BSE image of the reacted sample, captured under a resolution of 0.30 μ m; d) enlarged image of the reacted grain surfaces showing signs of dissolution. Subfigure (a) reproduced with permission from ref (40) 40. Copyright 2022 ACS Publications.

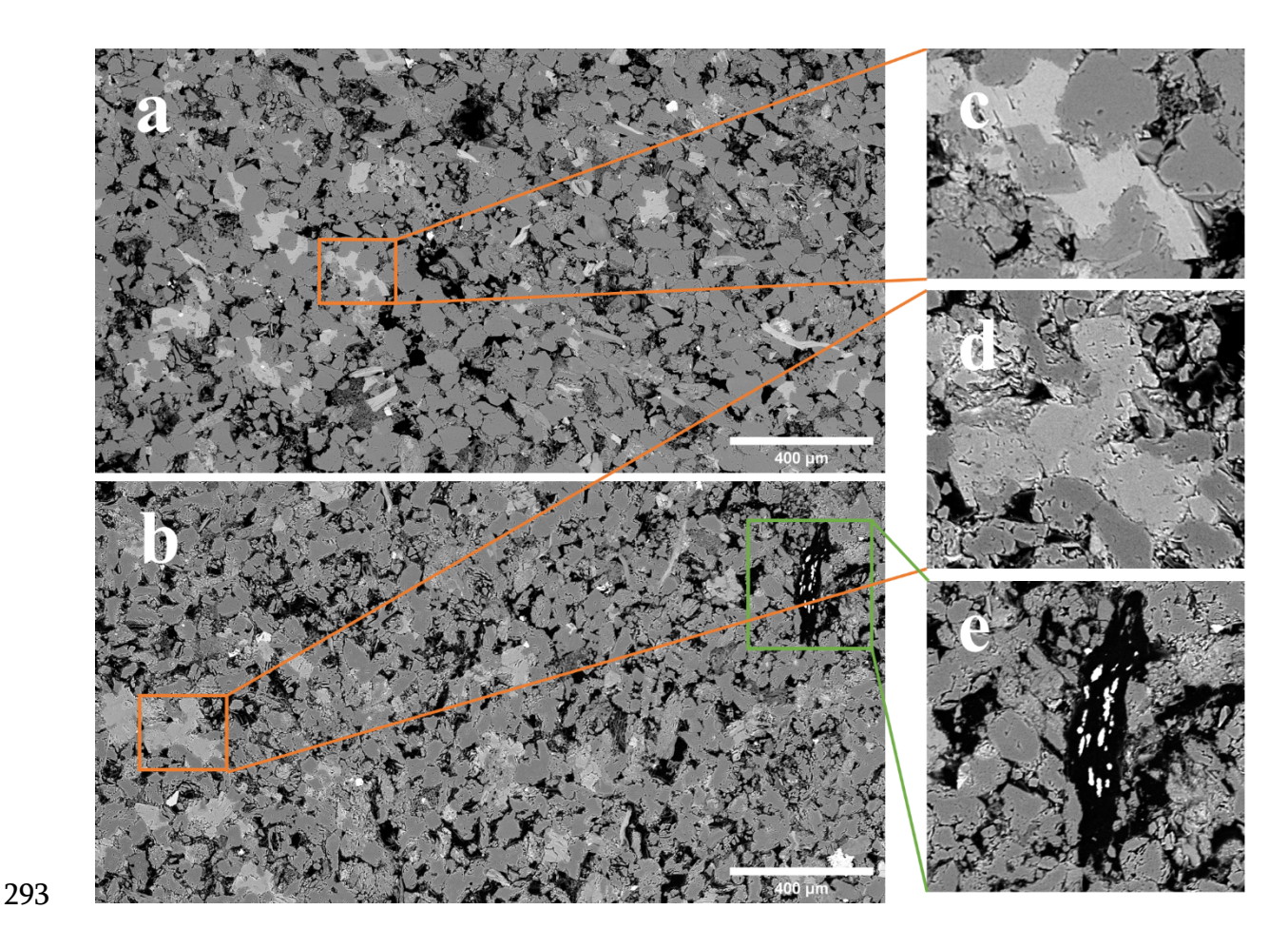


Figure 8. 2D BSE images of unreacted and reacted Bandera Grey sample thick sections: a) BSE image of the unreacted sample, captured under a resolution of 0.74 μ m; b) BSE image of the reacted sample, captured under a resolution of 0.74 μ m. Enlarged images of unreacted c) and reacted d), e) regions where increased grain roughness is evident. Image c) and d) highlight the evolution of carbonate grains (ankerite). Subfigure (a) reproduced with permission from ref (40) 40 . Copyright 2022 ACS Publications.

Images of the reacted samples, in general, show increased surface roughness (Figures 7, 8). In the zoomed-in images of the Kentucky samples, shown in Fig 7b and d, the dissolution of grain surfaces and mineral phases is observed, which could potentially increase the porosity as

well as pore connectivity. Prior to the core-flood dissolution experiment, the grains appear to have smooth surfaces and intact structures. In the image of the reacted sample (Figure 7c), additional roughness is evident on the surface of the grains. In addition, a large portion of some of the grains appears to be dissolved, which creates additional pore space. The same phenomenon can be observed in Figure 8, which shows the difference between the 2D BSE images of the Bandera Grey sample before and after experiments. The mineral surfaces appear to be rougher after the reaction; however, such change in surface roughness is only evident on quartz, and no distinct dissolution of the carbonate phase – ankerite is observed (Figures 8c and 8d). Pyrite is found to have dissolved during two weeks of reaction (Figure 8e).

The increase in mineral surface roughness was also noted in the quantitative results calculated from 3D X-ray CT images (Table 3). There is a slight increase in the porosity calculated from X-ray CT images for the Kentucky sandstone sample, where the images were captured in the same area of the core. The porosity increased from 10.73% to 13.23% after the core-flood experiment with a duration of 1 week (168 hours).

Opposite phenomena are observed between the results of porosity calculated from 2D SEM BSE images and 3D X-ray CT images. The porosity calculated from 2D SEM images of the unreacted Kentucky sample is higher than the reacted sample, 13.25% versus 10.73%. This may be due to the reason that the 2D SEM BSE images were not taken from the same sample/location, and the homogeneity of the pore distribution may vary among samples. Therefore, small variations in estimated porosity from 2D SEM BSE images are expected. However, the 3D X-ray CT images were captured in the same area of the core; thus, the

porosity estimated from the 3D X-ray CT images here is more representative than the porosity estimated from 2D SEM BSE images.

The connected surface area of the Kentucky sample calculated from 3D X-ray CT images increases where the resolution corrected surface area of the unreacted sample is $0.141~\text{m}^2/\text{g}$, and the reacted sample is $0.228~\text{m}^2/\text{g}$. This suggests the pore connectivity or the mineral surface roughness increased during the dissolution experiment. A similar increase in porosity and mineral surface area occurred for the Bandera Gray sample, where the porosity of the 3D image increased from 15.12% to 20.87%, and the resolution corrected connected surface area increased from $0.063~\text{m}^2/\text{g}$ to $0.085~\text{m}^2/\text{g}$.

3.2 Effluent sample analysis

3.2.1 Kentucky

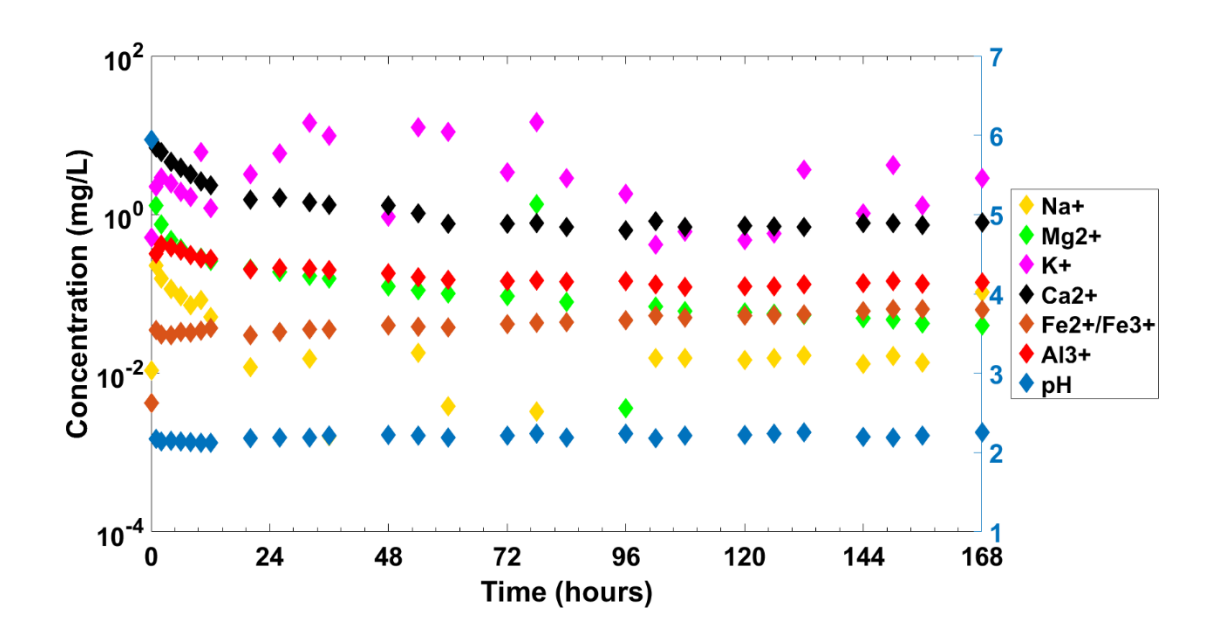


Figure 9. The evolution of the major ion concentrations in the effluent sample collected from the core-flood experiment with the Kentucky sample, data measured through ICP-OES.

The concentrations of major ions in the effluent sample collected during the 168-hour coreflood experiment are plotted in Figure 9. The initial peak of the calcium (Ca²+) and magnesium
(Mg²+) concentration (Figure 9, black and green data points) indicates that there is likely a
small amount of dolomite – CaMg(CO₃)² dissolution. Potassium (K+) and sodium (Na+) are
expected to result from the dissolution of clay minerals – smectite/illite. The dissolution of
feldspar minerals – K-feldspar and albite can also contribute to the release of potassium and
sodium ions; however, compared with clay smectite/illite, feldspars are chemically more stable
and therefore are expected to have lower reaction rates than smectite/illite. Aluminum (Al³+)
ions are expected to mainly come from the dissolution of feldspars (albite and K-feldspar) and
clay minerals (smectite/illite), but the dissolution of muscovite can also result in the increase
of aluminum concentration. Iron (Fe²+/3+) is expected to be released from the dissolution of
ilmenite. pH is also measured during the 168-hour period, where it remains stable at around

3.2.2 Bandera Grey

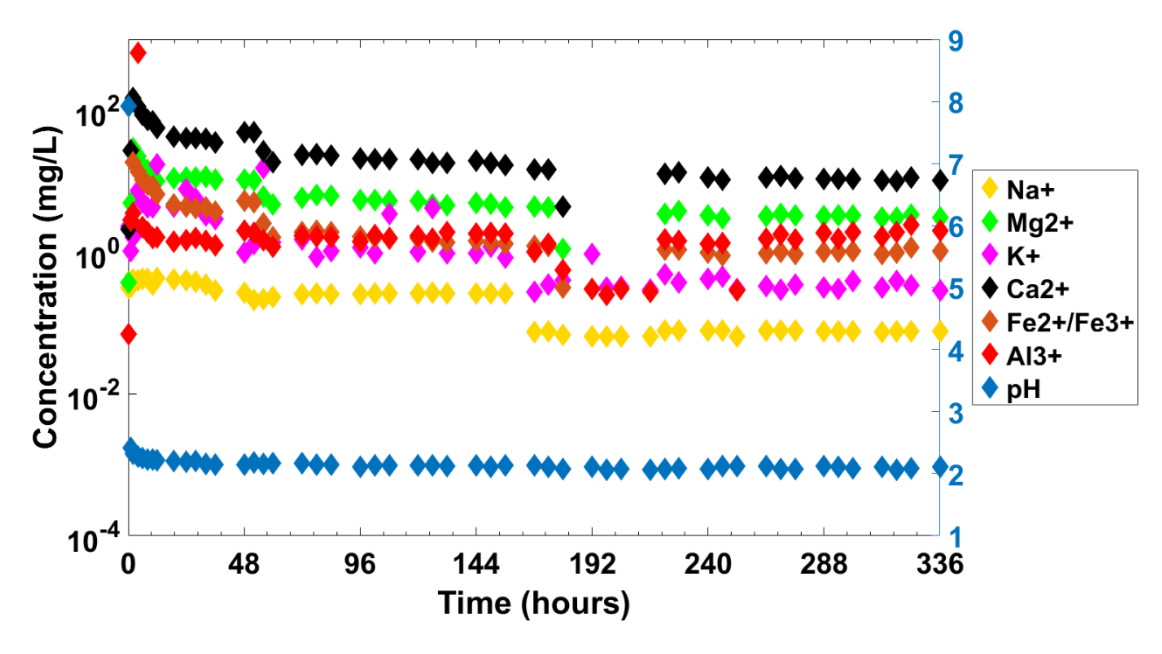


Figure 10. The evolution of the major ion concentrations in the effluent sample collected from the core-flood experiment with the Bandera Grey sample, data measured through ICP-OES.

The core-flood experiment for the Bandera Grey sample was carried out for two weeks – 336 hours. The pH was recorded, and effluent samples were collected at different time intervals. The initial pH of the system is 7.92, and it decreases to approximately 2.16 at 32 hours and starts to fluctuate between 2.06 and 2.18. The concentrations of major ions in effluent were measured using ICP_OES, and the results are plotted in Figure 10. Similar to the Kentucky sample (Figure 9), the dissolution of the carbonate mineral – ankerite results in the initially observed peak of calcium (Ca²⁺), magnesium (Mg²⁺), and iron (Fe²⁺/³⁺) concentrations (Figure 10, green, black, and brown data points). The concentrations of calcium (Ca²⁺), magnesium (Mg²⁺), and iron (Fe²⁺/³⁺) slowly decrease as the reaction proceeds. There is an apparent drop in the concentrations of these three ions between 180 to 192 hours. Between 192 to 216 hours,

no calcium (Ca^{2+}), magnesium (Mg^{2+}), and iron ($Fe^{2+}/^{3+}$) are measured; however, after 216 hours, they reappear at the same concentration level before the gap. This may reflect the inaccessibility of ankerite for reaction during that period of time and the creation of new pathways after 216 hours that reach ankerite surfaces, resuming ankerite dissolution. A similar phenomenon can be observed around 252 hours, where no calcium (Ca²⁺), magnesium (Mg²⁺), and iron (Fe²⁺/³⁺) are measured. Potassium (K⁺), sodium (Na⁺), and aluminum (Al³⁺) ions are expected to be coming from the dissolution of smectite/illite and feldspar minerals – K-feldspar and albite. After the initial peak, the concentration of these three ions decreases and remains relatively stable. At around 156 hours, there is a drop in potassium (K⁺) and sodium (Na⁺) concentration, which is 24 hours earlier than the concentration drop of calcium (Ca²⁺), magnesium (Mg²⁺), and iron (Fe²⁺/³⁺). However, the concentration of potassium (K⁺) and sodium (Na⁺) does not return to the previous level. The concentration of aluminum (Al³⁺) dropped around 180 hours, same as calcium (Ca²⁺), magnesium (Mg²⁺), and iron (Fe²⁺/³⁺), and returned to its previous concentration level around 216 hours.

365

366

367

368

369

370

371

372

373

374

375

376

377

378

379

380

381

Table 5. Mineral surface area acquired from imaging and manual calculation (equation 1). Manual calculations use the initial and final porosity & volume fraction measured from imaging and utilize the equation used in CrunchFlow simulation. VF – volume fraction, ASA – Accessible surface area.

Sample	Mineral	Initial	Final VF	Initial	Final	ASA	Final	SA
		VF		ASA (from	(from		(calculat	ed,
							m^2/g)	

				images, m²/g)	images, m²/g)	
	Quartz	54.44	47.19	4.73x10 ⁻⁰²	6.28x10 ⁻⁰²	3.49x10 ⁻⁰²
	K-feldspar	2.54	10.28	4.98x10 ⁻⁰³	2.56x10 ⁻⁰²	4.33x10 ⁻⁰³
	Albite	14.61	13.92	1.41x10 ⁻⁰²	2.03x10 ⁻⁰²	1.11x10 ⁻⁰²
Kentucky	Smectite/illite	10.21	6.02	NA	NA	NA
	Muscovite	2.22	7.01	NA	NA	NA
	Anatase	0.15	1.32	1.97x10 ⁻⁰⁴	1.31x10 ⁻⁰³	1.71x10 ⁻⁰⁴
	Quartz	53.94	56.61	3.85x10 ⁻⁰²	4.95x10 ⁻⁰²	3.10x10 ⁻⁰²
	K-feldspar	10.30	8.76	3.53x10 ⁻⁰³	2.46x10 ⁻⁰³	2.29x10 ⁻⁰³
	Albite	8.69	8.03	4.16x10 ⁻⁰³	3.43x10 ⁻⁰³	2.86x10 ⁻⁰³
	Ankerite	4.84	4.73	4.48x10 ⁻⁰⁴	6.81x10 ⁻⁰⁵	3.20x10 ⁻⁰⁴
Bandera	Smectite/illite	5.43	6.18	NA	NA	NA
Grey	Muscovite	0.58	0.02	NA	NA	NA
	Biotite	0.97	0.30	NA	NA	NA
	Anatase	0.24	0.20	6.31x10 ⁻⁰⁵	8.51x10 ⁻⁰⁶	5.09x10 ⁻⁰⁵

The evolution of accessible surface area determined from image analysis varies between Bandera Grey and Kentucky (Tables 2 and 4). Manual calculations (Table 5) have also been done, incorporating the data (porosity and volume fraction) acquired from imaging into equation 1 to calculate the final accessible surface area for each mineral phase. The computed final accessible surface areas of each mineral phase vary a lot from the accessible surface area estimated from imaging. The calculated final accessible surface areas for all mineral species in the Kentucky sample decreased; however, the estimated image obtained accessible surface area

increased. For Bandera Grey, the calculated final surface areas of all minerals decrease, while it decreases for all minerals except quartz for the image obtained accessible surface area.

4. Discussion

391

392

393

394

395

396

397

398

399

400

401

402

403

404

405

406

407

408

409

410

Mineral surface roughness and pore connectivity increased during the 168-hour core-flood dissolution experiment with 0.01M hydrochloric acid (pH = 2). The overall dissolution reaction rates and extent are expected to be low as no distinct differences were observed before and after the experiment from both BSE and X-ray CT images. Porosity calculated from 3D X-ray CT images confirmed the increase in porosity and accessible surface area of almost all minerals by 1-2 orders of magnitude after the reaction. This is due to the overall increase in the total connected surface area calculated from 3D X-ray CT images. This increase results from increased roughness and/or pore connectivity. A noted increase in roughness was also evident in the 2D SEM images of the reacted samples. The total connected surface area of the two samples both increased after core-flood experiments. For the Kentucky sample, the total connected surface area increased from 0.14 to 0.23 m²/g (64% increase), whereas the total connected surface area of the Bandera Grey sample only increased from 0.063 to 0.085 m²/g (35% increase). The large difference in the total connected surface area change is likely the reason that the estimated accessible surface area of all mineral phases in Kentucky increased, whereas, in the Bandera Grey sample, only the accessible surface area of quartz increased. Before the reaction, the common four mineral phases that are found in both samples - quartz, K-feldspar, albite, and anatase have similar

accessible surface areas. However, after the reaction, the accessible surface areas of these four mineral phases in the Kentucky sample are distinctly larger than in the Bandera Grey sample. The 64% increase in the total connected surface area of the Kentucky core sample is expected to be the result of porosity increase and pore connectivity increase where new pathways are formed. This is also evident from the X-ray CT images where connectivity increased from 74% to 81% for Kentucky. Whereas in the Bandera Grey sample, the total connected surface area only increased by 35%. In this case, there is an increase in pore connectivity; however, that is much lower than in the Kentucky sample. In the Bandera Grey sample, the mineral surfaces that were initially accessible to the reacting flow are likely to become rough as reactions progress. As for the increased accessible surface area of quartz in the Bandera Grey sample, this is expected to be the result of increased surface roughness (Figure 8) and/or new surface of quartz being exposed to reacting flow due to the dissolution of the mineral phases that were initially covering quartz grains (e.g., smectite/illite). With higher accessible surface areas in the Kentucky sample, the effluent ion concentrations are anticipated to be higher. However, comparing results in Figures 9 and 10, the observed effluent ion concentrations are generally higher in the Bandera Grey sample. This is perhaps due to differences in the overall pore volume of the two samples as well as variations in the compositon of the accessible mineral surface areas between the two samples. Comparing the BSE and X-ray CT images of the two samples, it can be observed that Bandera Grey sample has not only higher porosity but also higher pore connectivity and pore volume. In the Kentucky

411

412

413

414

415

416

417

418

419

420

421

422

423

424

425

426

427

428

429

430

sample, the overall porosity, pore connectivity, and pore volume are smaller. A smaller pore volume yields a lower water-rock ratio and thus lower driving force for the reaction and quicker approach to equilibrium. This would limit the sustained rate of reaction.

432

433

434

435

436

437

438

439

440

441

442

443

444

445

446

447

448

449

450

451

452

The observed dissolution rate depends not only on total accessible surface area but the composition of the surface. Both of the unreacted samples are comprised of similar fractions of quartz, feldspar and clay minerals, albeit the Bandera Gray sample additionally has a carbonate mineral. However, the heterogeneous distribution of clay minerals may play a significant role in the observed reaction rates. For example, in Figures 9 and 10, the fluctuation of potassium (K+) concentration is likely due to dissolution of clay minerals – smectite/illite. Initially, not all of smectite/illite is exposed (accessible) to the connected pore spaces. As the reaction proceeds, connected pore spaces might be expanded, new flow paths formed, and more smectite/illite accessible to the reacting fluid, thus, yielding higher observed effluent ion concentrations for a period of time. The dissolution rate of mineral phases also needs to be considered and can vary orders of magnitude between phases. Under low pH conditions, carbonate minerals, such as ankerite observed in the Bandera Gray sample, will rapidly dissolve. This may additionally explain the observed higher effluent ion concentrations for this sample as approximately 47.5% of the surface in the unreacted Kentucky sample is comprised of less reactive smectite compared to around 26% for Bandera Grey. Having most of the total connected surface comprising of smectite, which has a lower dissolution rate than the carbonate mineral phases⁴¹, results in lower ion concentrations in the effluent from the core flood experiment.

Understanding the evolution of mineral surface area is challenging. The way of currently modeling mineral surface areas evolution has its advantages as well as limitations. In CrunchFlow, for example, the mineral surface area is estimated from the evolution of porosity and mineral volume fraction. This is a relatively efficient approach as porosity, and mineral volume fraction can be measured relatively easily without image processing, e.g., via Mercury Intrusion Porosimetry (MIP) or X-ray diffraction (XRD). It can also be utilized to validate experimental data such as the change of porosity, mineral volume fraction, and mineral surface area. However, the model represents a relatively more homogeneous environment compared to the core sample used in the experiment. For instance, a heterogeneous distribution of minerals could have one group of minerals concentrated in one area of the sample, and flow paths might evolve as reactions proceed. As such, the accessibility in different regions could vary over time, such as the change of the concentration observed in Figure 10. These phenomena are difficult to incorporate into current continuum scale model approaches.

5. Conclusions

This work provides insight into how accessible mineral surface areas change in core-flood dissolution experiments. Mineral dissolution was evident in both the Kentucky and Bandera Gray samples after exposure to acidic solution. Reactions resulted in an increase in mineral surface roughness, porosity, pore connectivity and surface area in both samples. Compared to the Kentucky sample, the Bandera Grey sample has a higher porosity and carbonate content and is thus expected to be more reactive to the acidic fluid. However, quantitative analysis from 2D and 3D imaging suggests that the Kentucky sample had a larger change in overall pore

connectivity, which resulted in an 64% increase in the observed total connected surface area after reaction compared to the 35% increase observed in the Bandera Gray sandstone. This resulted in a substantial change in the observed accessible mineral surface areas for the minerals.

A comparison of the evolution of accessible mineral surface areas for phases observed in both samples reveals that accessible mineral surface areas can increase or decrease due to reactions (Table 5). In the Kentucky sandstone, mineral accessible surface areas increased for all minerals with large (more than one order of magnitude) increases observed for the K-feldspare and anatase minerals. Conversely, eeductions in accessible surface areas of anatase and ankerite of one order of magnitude were observed in the Bandera Gray sample. This indicates that the evolution of mineral accessible surface area is likely sample-specific rather than mineral-specific. The evolution of accessible mineral surface area is largely impacted by the total connected surface area as well as pore connectivity. This was also observed in a previous study done by Salek et al. (2022)⁴⁰, where they worked on seven different sandstone samples.

In summary, mineral surfaces appear rougher after reacting with hydrochloric acid. Under the same experimental conditions, the accessible mineral surface area of a mineral phase can either decrease or increase depending on the sample pore connectivity change. The accessible mineral surface area tends to increase in samples with greater increases in pore connectivity after reactions. The change in pore connectivity might not only be associated with whether a sample has larger amounts of reactive minerals but also with the distribution of that mineral where the compostion of the pore-mineral interface is critical in the observed extent of

reaction. Variations in pore connectivity that impact the evolution of accessible mineral surface area are not captured by simple relationships for mineral surface area evolution that are commonly used in reactive transport models. While calculated discrepancies in mineral surface area were often within the same order of magnitude, some were greater than one order of magnitude, which will largely impact simulated mineral reaction rates.

Acknowledgment

495

496

497

498

499

500

505

507

508

501 This work is supported by the National Science Foundation under Grant No. EAR-1847243. 502 Purchase of the X-ray Computed Tomography instrument used to obtain results included in 503

this publication was supported by the National Science Foundation under the award CMMI

MRI 1919818. 504

Supporting Information

506 3D X-ray CT images of Kentucky and Bandera Gray core samples before and after the core-

flood experiment

Abbreviations and Terminologies

- 509 SEM - Scanning Electron Microscopy
- 510 3D X-Ray nano-CT - Three-dimension X-Ray nano Computed Tomography
- 511 BET - Brunauer–Emmett–Teller
- 512 XRD - X-ray Diffraction
- 513 SSA (m²/g) - Specific Surface Area

- ASA (m²/g) Accessible Surface Area, the mineral surface area accessible to pore fluids
- 515 CF Correction factor, applied to account for the sub-resolution features in 3D X-ray nano-
- 516 CT images
- Mineral Accessibility (%) Fraction of pore-grain interfacial pixels of each mineral phase
- Porosity (%) The ratio of void space to the total volume
- 519 Connected porosity (%) The ratio of connected pore space to the total volume
- 520 Total Connected Surface Area (m²/g)- Total mineral surface area adjacent to connected pores

522 References

- Hänchen, M., Prigiobbe, V., Baciocchi, R. & Mazzotti, M. Precipitation in the Mgcarbonate system—effects of temperature and CO2 pressure. *Chem Eng Sci* **63**, 1012–
- 525 1028 (2008).
- 526 2. Schaef, H. T. & McGrail, B. P. Dissolution of Columbia River Basalt under mildly acidic
- 527 conditions as a function of temperature: Experimental results relevant to the geological
- 528 sequestration of carbon dioxide. *Applied Geochemistry* **24**, 980–987 (2009).
- 529 3. Wilkin, R. T. & DiGiulio, D. C. Geochemical impacts to groundwater from geologic
- 530 carbon sequestration: controls on pH and inorganic carbon concentrations from reaction
- path and kinetic modeling. Environ Sci Technol 44, 4821–4827 (2010).
- 532 4. Shao, H., Ray, J. R. & Jun, Y.-S. Effects of salinity and the extent of water on supercritical
- 533 CO2-induced phlogopite dissolution and secondary mineral formation. *Environ Sci*
- 534 *Technol* **45**, 1737–1743 (2011).
- 535 5. Tutolo, B. M., Luhmann, A. J., Kong, X.-Z., Saar, M. O. & Seyfried Jr, W. E. CO2
- sequestration in feldspar-rich sandstone: coupled evolution of fluid chemistry, mineral
- reaction rates, and hydrogeochemical properties. *Geochim Cosmochim Acta* **160**, 132–
- 538 154 (2015).
- 6. Cui, G., Zhu, L., Zhou, Q., Ren, S. & Wang, J. Geochemical reactions and their effect on
- 540 CO2 storage efficiency during the whole process of CO2 EOR and subsequent storage.
- International Journal of Greenhouse Gas Control 108, 103335 (2021).

- 542 7. Qin, F. & Beckingham, L. E. The impact of mineral reactive surface area variation on
- simulated mineral reactions and reaction rates. Applied Geochemistry 124, 104852
- 544 (2021).
- 545 8. Khurshid, I. & Afgan, I. Geochemical Investigation of CO2 Injection in Oil and Gas
- Reservoirs of Middle East to Estimate the Formation Damage and Related Oil Recovery.
- 547 Energies (Basel) **14**, 7676 (2021).
- 548 9. Ma, J., Ahkami, M., Saar, M. O. & Kong, X.-Z. Quantification of mineral accessible
- surface area and flow-dependent fluid-mineral reactivity at the pore scale. *Chem Geol*
- **563**, 120042 (2021).
- 551 10. Algive, L., Békri, S., Nader, F. H., Lerat, O. & Vizika, O. Impact of diagenetic alterations
- on the petrophysical and multiphase flow properties of carbonate rocks using a reactive
- pore network modeling approach. Oil & Gas Science and Technology-Revue d'IFP
- 554 Energies nouvelles **67**, 147–160 (2012).
- 555 11. Beckingham, L. E., Peters, C. A., Um, W., Jones, K. W. & Lindquist, W. B. 2D and 3D
- imaging resolution trade-offs in quantifying pore throats for prediction of permeability.
- 557 *Adv Water Resour* **62**, 1–12 (2013).
- 558 12. Nogues, J. P., Fitts, J. P., Celia, M. A. & Peters, C. A. Permeability evolution due to
- dissolution and precipitation of carbonates using reactive transport modeling in pore
- networks. Water Resour Res 49, 6006–6021 (2013).
- 561 13. Zhang, L., Soong, Y., Dilmore, R. & Lopano, C. Numerical simulation of porosity and
- permeability evolution of Mount Simon sandstone under geological carbon
- sequestration conditions. *Chem Geol* **403**, 1–12 (2015).
- 564 14. Al-Yaseri, A. et al. Permeability evolution in sandstone due to CO2 injection. Energy &
- 565 *Fuels* **31**, 12390–12398 (2017).
- 566 15. Noiriel, C. & Daval, D. Pore-scale geochemical reactivity associated with CO2 storage:
- new frontiers at the fluid–solid interface. *Acc Chem Res* **50**, 759–768 (2017).
- 568 16. Carroll, S., Hao, Y., Smith, M. & Sholokhova, Y. Development of scaling parameters to
- describe CO2-rock interactions within Weyburn-Midale carbonate flow units.
- 570 International Journal of Greenhouse Gas Control 16, S185–S193 (2013).
- 571 17. Navarre-Sitchler, A. K. et al. Porosity and surface area evolution during weathering of
- two igneous rocks. *Geochim Cosmochim Acta* **109**, 400–413 (2013).
- 573 18. Luhmann, A. J. et al. Permeability, porosity, and mineral surface area changes in basalt
- 574 cores induced by reactive transport of CO 2-rich brine. *Water Resour Res* **53**, 1908–1927
- 575 (2017).

- 576 19. Přikryl, J., Jha, D., Stefánsson, A. & Stipp, S. Mineral dissolution in porous media: An experimental and modeling study on kinetics, porosity and surface area evolution.
- 578 *Applied Geochemistry* **87**, 57–70 (2017).
- 579 20. Yang, Y., Bruns, S., Stipp, S. L. S. & Sørensen, H. O. Impact of microstructure evolution
- on the difference between geometric and reactive surface areas in natural chalk. Adv
- 581 *Water Resour* **115**, 151–159 (2018).
- 582 21. Noiriel, C. et al. Changes in reactive surface area during limestone dissolution: An
- 583 experimental and modelling study. *Chem Geol* **265**, 160–170 (2009).
- 584 22. Israeli, Y. & Emmanuel, S. Impact of grain size and rock composition on simulated rock
- weathering. *Earth Surface Dynamics* **6**, 319–327 (2018).
- 586 23. Noiriel, C., Gouze, P. & Bernard, D. Investigation of porosity and permeability effects
- from microstructure changes during limestone dissolution. *Geophys Res Lett* **31**, (2004).
- 588 24. Steefel, C. I. et al. Reactive transport codes for subsurface environmental simulation.
- 589 *Comput Geosci* **19**, 445–478 (2015).
- 590 25. Lichtner, P. C. The quasi-stationary state approximation to coupled mass transport and
- fluid-rock interaction in a porous medium. Geochim Cosmochim Acta 52, 143–165
- 592 (1988).
- 593 26. Emmanuel, S. & Berkowitz, B. Mixing-induced precipitation and porosity evolution in
- 594 porous media. *Adv Water Resour* **28**, 337–344 (2005).
- 595 27. Peters, C. A. Accessibilities of reactive minerals in consolidated sedimentary rock: An
- imaging study of three sandstones. *Chem Geol* **265**, 198–208 (2009).
- 597 28. Landrot, G., Ajo-Franklin, J. B., Yang, L., Cabrini, S. & Steefel, C. I. Measurement of
- accessible reactive surface area in a sandstone, with application to CO 2 mineralization.
- 599 *Chem Geol* **318–319**, 113–125 (2012).
- 600 29. Beckingham, L. E. et al. Evaluation of accessible mineral surface areas for improved
- prediction of mineral reaction rates in porous media. *Geochim Cosmochim Acta* **205**,
- 602 31–49 (2017).
- 603 30. Brunhoeber, O. M., Anovitz, L. M., Asadi, P. & Beckingham, L. E. Role of mineralogy
- in controlling fracture formation. ACS Earth Space Chem 5, 3104–3114 (2021).
- 605 31. Dove, P. M., Han, N. & de Yoreo, J. J. Mechanisms of classical crystal growth theory
- 606 explain quartz and silicate dissolution behavior. *Proceedings of the National Academy*
- 607 of Sciences **102**, 15357–15362 (2005).

- 608 32. Bibi, I., Arvidson, R. S., Fischer, C. & Lüttge, A. Temporal evolution of calcite surface dissolution kinetics. *Minerals* **8**, 256 (2018).
- Mouzakis, K. M. *et al.* Experimental study of porosity changes in shale caprocks exposed to CO2-saturated brines I: Evolution of mineralogy, pore connectivity, pore size distribution, and surface area. *Environ Eng Sci* **33**, 725–735 (2016).
- 613 34. Scislewski, A. & Zuddas, P. Estimation of reactive mineral surface area during water– 614 rock interaction using fluid chemical data. *Geochim Cosmochim Acta* **74**, 6996–7007 615 (2010).
- Beckingham, L. E. *et al.* Evaluation of accessible mineral surface areas for improved prediction of mineral reaction rates in porous media. *Geochim Cosmochim Acta* (2017) doi:10.1016/j.gca.2017.02.006.
- 619 36. Qin, F. & Beckingham, L. E. Impact of image resolution on quantification of mineral abundances and accessible surface areas. *Chem Geol* **523**, 31–41 (2019).
- 621 37. Asadi, P. & Beckingham, L. E. Integrating Machine/Deep Learning Methods and 622 Filtering Techniques for Reliable Mineral Phase Segmentation of 3D X-ray Computed 623 Tomography Images. *Energies (Basel)* **14**, 4595 (2021).
- Awolayo, A. N. *et al.* Mineral surface area accessibility and sensitivity constraints on carbon mineralization in basaltic aquifers. *Geochim Cosmochim Acta* **334**, 293–315 (2022).
- 627 39. Qin, F. *et al.* Estimation of Mineral Accessible Surface Area from Mineral Abundance and Clay Content. *ACS Earth and Space Chem* (2023).
- Salek, M. F. *et al.* Impact of Pore Connectivity on Quantification of Mineral Accessibility in Sandstone Samples. *ACS Earth Space Chem* 6, 1858–1867 (2022).41.
 Brantley, S L. Kinetics of mineral dissolution. *Kinetics of water-rock interaction*, 151-210 (2008).